PLASMA DYNAMICS

XI. PLASMA PHYSICS*

Academic and Research Staff

Prof. S. C. Brown
Prof. W. P. Allis
Prof. J. C. Ingraham
Dr. G. Lampis
J. J. McCarthy
E. M. Mattison
W. J. Mulligan

Graduate Students

M. L. Andrews
D. L. Flannery
E. V. George
P. W. Jameson
R. L. Kronquist
D. T. Llewellyn-Jones
G. L. Rogoff
J. K. Silk
D. W. Swain
F. Y-F. Tse

A. ELECTROMECHANICAL DEVICE TO FEED EXPERIMENTAL DATA AUTOMATICALLY INTO A TIME-SHARED COMPUTER SYSTEM – I.†

This report describes the purpose and principles of operation of the device that has been built. A succeeding report will describe in detail the construction of the device and its performance under actual operating conditions.

1. Introduction

An important area of application of the project MAC (Machine Aided Cognition – Multiple Access Computer) Compatible Time-Sharing System is in conjuction with external laboratory experiments, particulary those in the physical sciences. Here the experimenter, with a CTSS terminal next to his apparatus, can enjoy the luxury of an on-line computer for processing his experimental data as they are produced. In many cases the ability to feed the data into the computer automatically is highly desirable. This report describes a simple homemade device that can insert BCD (Binary Coded Decimal) data – in the present case generated in parallel form by a digital voltmeter (DVM) – into a Type 33KSR teletype terminal at rates up to the maximum of 10 characters per second allowed by the telephone lines, data sets, and so forth. Such a device could find application in many areas of physics, physical chemistry or engineering, where an experiment produces data at a rate no faster than, for example, one 6-digit number per second.

2. The Code

The signal sent to the computer by the teletype and data set consists of a series of square pulses at 110 cps, i.e., a voltage alternating between two discrete levels, "mark" and "space." When no signal is being sent, the data-set output remains at the

*This work was supported by the United States Atomic Energy Commission (Contract AT(30-1)-1842).

†The work reported here was supported, through access to its computer facilities, by Project MAC, an M. I. T. research program sponsored by the Advanced Research Agency, Department of Defense, under Office of Naval Research Contract Nonr-4102(01).

When no signal is being sent, the data-set output remains at the "mark" voltage level.

One character in teletype code consists of 11 bits, each one of which is either a mark or a space of 1/110 sec ≈ 9 msec duration. The first, or "start," bit of every character is a space. Eight information bits follow, then two "end" bits, which are always "marks." To avoid confusion, the 11 bits constituting the entire character will be referred to as C-bits, and the 8 information bits will be referred to as I-bits. Thus the first I-bit is the second C-bit, and so on.

In the teletype code used by Project MAC, every character has a "mark" for the eighth I-bit (ninth C-bit). Moreover, all numerals have the same configuration for I-bits 5-7, differing only in the first four I-bits. Since C-bit 1 is always a space, C-bits 9, 10, and 11 are always marks, and C-bits 6-8 are the same for all numerals, only C-bits 2-5 need be provided to specify a numeral, C-bits 1 and 6-11 remaining permanently set.

3. Teletype

Figure XI-1 is a simplified diagram of the hardware configuration. The teletype consists of three basic units: keyboard, printer, and data set.

When a key is depressed on the keyboard, a single-pole double-throw relay (hereafter called the "main relay") produces a series of contact closures that send to the printer a sequence of "mark" and "space" voltages in the appropriate character code

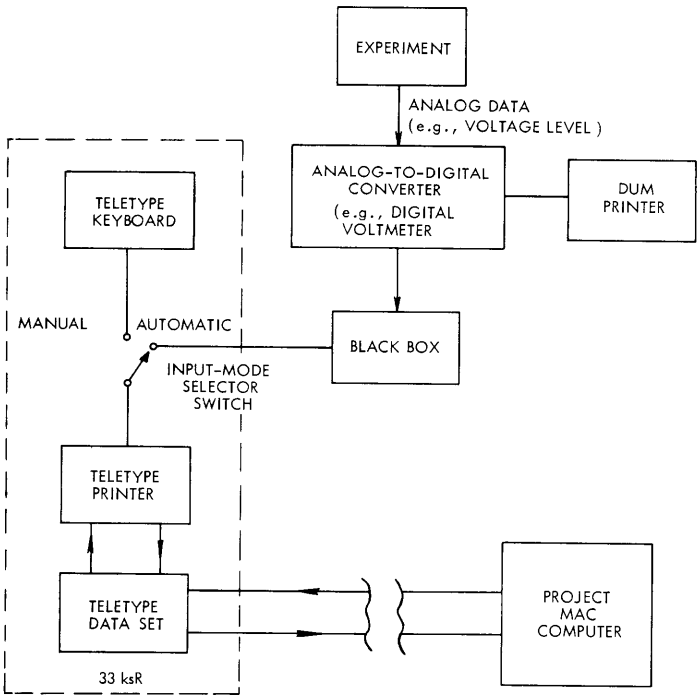

Fig. XI-1. Simplified schematic of experimental computer system.

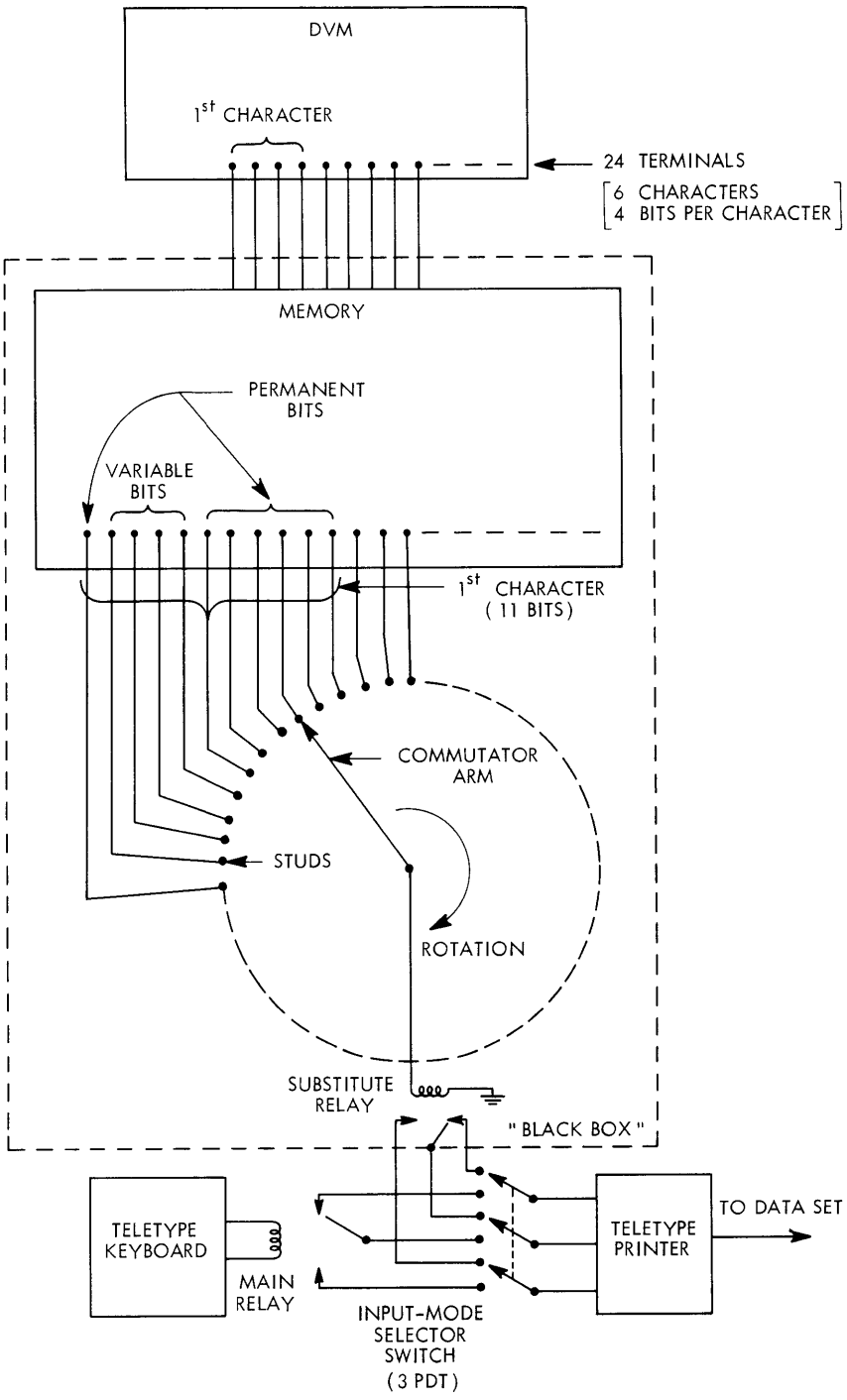

Fig. XI-2. Detail of the "Black Box."

and at the proper rate. The data set then sends the character to the computer, while the printer types it on paper.

The data to be input to the computer is produced by the DVM in the form of a printed paper tape and BCD-coded voltages. Heretofore the data have been read from the tape and typed manually into the keyboard. At present, the equipment accepts the data in electrical form and feeds it directly to the printer and data set. The switch between the keyboard and printer replaces the main relay by a similar SPDT relay actuated by the black box, enabling the black box to act as an "automatic keyboard." Because the black box feeds the printer, a written record of the data is obtained at the same time as they are sent to the computer.

4. The Black Box

This device is essentially a serializer. The data bits, in the form of positive- or zero-voltage levels, are presented to it simultaneously. In the present application there are 4 bits per character: 1-2-4-8-BCD code. This string of 11 pulses, each of 9-msec duration, actuates the SPDT relay, which substitutes for the main relay and hence for the keyboard.

The parallel set of bits from the DVM is inserted, upon an appropriate command, into a memory, which is sampled sequentially by a commutator. The memory is necessary because the DVM presents the information for only a few milliseconds, whereas the time required to send the data through the teletype equals the number of characters $\times$ 0.1 second per character. (Time per character = bits $\times$ 9 msec/bit.)

Figure XI-2 shows how the information is removed serially from the memory and sent to the teletype. The memory consists of 24 SPDT latching (bistable) reed relays, whose arms are connected to the commuter studs. The memory relays place on the studs "marks" and "space" voltages, which are seen sequentially by the commutator and applied to the "substitute" relay. The last relay is also a latching reed relay; it holds each bit ("mark" or "space") until the following stud is sampled.

As mentioned before, C-bits 2-5 are the only ones that change during the transmission of numerical information. Thus C-bits 1 and 6-11 are "dummies" in the memory, permantly set at the appropriate voltages.

5. The Commutator

The commutator arm is driven by a 60-cpm synchronous electric motor to which it is connected by an electric clutch and brake. When the DVM presents the data it issues a "print" command pulse, primarily to actuate the DVM printer. The present device uses this pulse to: (a) connect the memory to the DVM; and (b) de-energize the brake and engage the clutch.

The commutator shaft has a cam which, upon completion of each revolution:

(a) disengages the clutch and energizes the brake; and (b) clears the memory. Thus the device as a whole has a duty cycle of just over one second (the time for revolution of the commutator shaft).

A more detailed description of the construction of this device, and a report on its performance under working conditions will appear subsequently.

D. T. Llewellyn-Jones, E. M. Mattison

B. DIFFUSION WAVES IN HOLLOW-CATHODE ARC

Attempts are being made to excite sinusoidal plasma density perturbations at the cathode of a hollow-cathode discharge. The resulting diffusion waves will be studied and should give data from which the effective diffusion coeffieients, $D_\perp$ and $D_\parallel$, of the highly ionized dense plasma may be determined.

The theory of diffusion waves was developed by Golubev[1] and successfully used by him to measure diffusion coefficients in a slightly ionized plasma in a magnetic field.[2] The results were in good agreement with classical neutral-dominated ambipolar diffusion theory. The present work is directed toward applying this diagnostic technique to a highly ionized (>30%), dense ($n>10^{13}$ cm^{-3}) plasma, in which enhanced diffusion may occur. The plasma is assumed to be characterized by the two ambipolar coefficients, $D_\perp$ and $D_\parallel$, and the diffusion equation is solved in cylindrical coordinates with the requirement of sinusoidal time dependence and complex exponential axial (x) dependence. The resulting separated-variables equation for the transverse coordinate function $R(\vec{r}_\perp)$ is a Helmholtz equation. A discrete infinity of R solutions, or transverse modes, exists, each having a different z-dependence through the separation constant. For a cylinder, the R functions are the Bessel functions forced to zero at the plasma boundary and multiplied by an azimthal function of the form $e^{im\phi}$. The unique solution (mode amplitudes) is fixed by superimposing modes to match the boundary conditions at the ends of the cylinder. Golubev had a plasma source at one end, and his tube was long enough to approximate a semi-infinite cylinder so that the boundary condition at the other end was essentially "no reflected waves." The dependence of each mode is

$$n_j(r,\phi,z,t) = A_j R_j(r,\phi)\ \mathrm{Re}\{e^{j\omega t-\gamma z}\},$$

where $\gamma_j \equiv \pm\left(\frac{D_\perp \beta_j^2 + i\omega}{D_\parallel}\right)^{1/2}$; A_j is mode amplitude; β_j^2 is the separation constant determined for the mode. For example, β is (2.4/R) for the first J_o mode. The real part of γ is the axial decay rate, and the imaginary part of γ is the wave number for spatial oscillation in the axial direction. Since we do not expect growing diffusion solutions, the sign of the real part of γ must always be chosen to give decay in the geometry that is being used.

Since the decay rate increases with β_j, the mode with smallest β will dominate the solution for large z, regardless of the form of the excitation at z = 0. In the Golubev experiments this was true at points more than two diameters from the source. In the high-frequency limit, $\omega \gg D_\perp \beta_j^2$, we have

$$\gamma_j = \sqrt{\frac{\omega}{2D_{||}}}\,(1 + i).$$

The decay rate and wave number are equal and do not depend on $D_\perp$ or β_j, and thus are the same for all modes. This is the familiar result for one-dimensional diffusion waves, and quite naturally may also be viewed as the limit of small $D_\perp$, where axial motion predominates. For $\omega \ll D_\perp \beta_j^2$, we have

$$\gamma_j = \beta_j \sqrt{\frac{D_\perp}{D_{||}}}.$$

The wave number is zero and pure decay results. The solution is essentially a slowly varying static diffusion solution. Under suitable conditions, the measurements of the decay lengths in the two limits can yield the values of $D_\perp$ and $D_{||}$. An important advantage of this method is that amplitude decay, rather than phase shift, is measured, since the latter is usually more difficult to measure accurately.

Since the cathode is believed to be a major source of plasma in the HCD, the device should be good for diffusion-wave studies, provided a suitable method can be found to modulate the plasma production rate at the cathode. This is being attempted at present.

Several problems inherent in the HCD device will complicate the diffusion wave theory needed to go with this experiment. The present geometry is a cylinder with L/D less than four; the length being limited by available magnetic field structure. The diameter could be decreased, but this would introduce other problems, such as pressure gradients casued by discharge pumping, and a column too thin for existing microwave diagnostics. Also, the plasma itself is a complicating factor. Since it is highly ionized, the diffusion coefficients depend on plasma density and therefore on position. Thermal gradients and diffusion are also present. There is a beam of streaming electrons from the cathode, although the bulk of electrons is contained in a Maxwellian distribution.

This work will continue with the goal of obtaining accurate measurement of effective diffusion coefficients in a highly ionized magnetically confined plasma in which enhanced or anomalous diffusion may exist.

D. L. Flannery

References

1. V. S. Golubev and V. A. Granovskii, Radio Engineering and Electronics (USSR) 7, 624 (1962).

2. V. S. Golubev, Soviet Physics – JETP 16, 1399 (June 1963).

C. SPATIALLY RESOLVED MEASUREMENTS OF EMISSION LINE PROFILES

1. Introduction

This report presents calculations of the performance of the optical system to be used in measurements of spectral-line profiles emitted by the hollow-cathode arc discharge. A Fabry-Perot etalon is to be used in the measurements. The computations presented here were performed to investigate the application of the optical system to spatially resolved measurements of line profiles.

An interferometer was chosen for this work because it provides high wavelength resolution, compact size, and relatively large aperture. The initial measurements will be performed with the use of a helium plasma, because of the large Doppler breadth of helium emission lines. Further experiments are planned with other gases to which small concentrations of helium have been added.

The optical system that will be used in the experiment consists of two lenses, the interferometer, and a pinhole. Light from the plasma is collected by the first lens, passes through the Fabry-Perot, and is focussed by the second lens on a pinhole. The light passing through the pinhole is detected by a photomultiplier.

This report presents a calculation of the fraction of light from a point source transmitted by the optical system as a function of the position of the source. The result of the computation is used to determine the performance of the optical system in spatially resolved measurements on nonuniform plasmas. For simplicity, the effects of the Fabry-Perot are assumed to be negligible and the calculations are made for a system of two lenses and a pinhole.

2. Computation of the Transmission Function

The computation presented here is that of the transmission function of the optical system shown in Fig. XI-3. The transmission function gives the fraction of the light

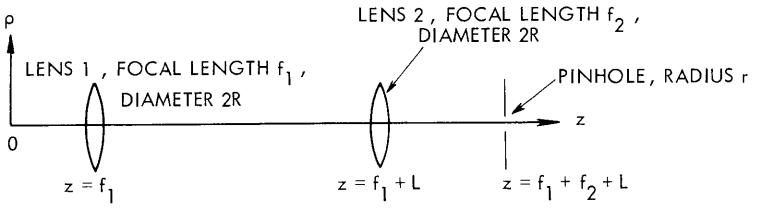

Fig. XI-3. Optical system.

intensity from an isotropically emitting point source which is transmitted by the optical system as a function of the position of the source. First, it is shown that rays passing through a small disk in the focal plane of Lens 1 are transmitted without loss. Then

this information is used to derive an expression for the transmission function. Finally, an approximate expression for the transmission function is obtained which is valid for typical geometrical conditions.

a. Full-Transmission Disk

Rays passing through a small disk in the focal plane of Lens 1 are transmitted by the optical system without loss. To determine the size of this disk, consider a point source in the focal plane of Lens 1 at a distance ρ_o from the axis. The rays from this source passing through Lens 1 form a parallel beam in the region between the two lenses. The rays are not parallel to the axis. Their slope can be determined immediately from the construction shown in Fig. XI-4. Ray 1, which is parallel to the axis before it reaches Lens 1, is refracted by that lens and passes through the focal point of the lens at $z = 2f_1$. Ray 2, which passes through the center of Lens 1 without deviation, is

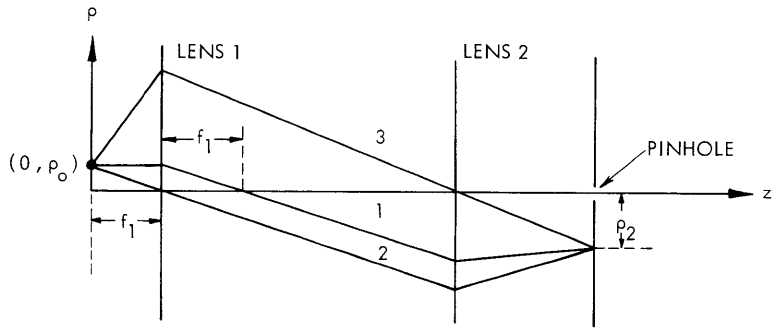

Fig. XI-4. Ray tracing for off-axis point in the focal plane of Lens 1.

parallel to Ray 1. Since these two rays are parallel, all other rays from the source at ρ_o are parallel.

The light from the source at $(0, \rho_o)$ that reaches Lens 2 will be focussed at a point in the focal plane of the lens at $z = f_1 + f_2 + L$. The ρ coordinate of the focus can be found by considering Ray 3, which passes through the center of Lens 2 without deviation. It reaches the plane $z = f_1 + f_2 + L$ at $\rho = -\rho_2 = -\rho_o f_2/f_1$. Thus all the light from the source at $(0, \rho_o)$ is focussed at $(f_1+f_2+L, -\rho_2)$ and is transmitted if $(\rho_o f_2/f_1) < r$, that is,

$$\rho_o < \frac{f_1}{f_2} r,$$

where r is the pinhole radius at $z = f_1 + f_2 + L$. No light goes through if $\rho_o > (f_1 r/f_2)$.

Note that in this calculation it is assumed that all light from the source passing through Lens 1 also passes through Lens 2. This is not quite correct because the light

beam that reaches the plane of Lens 2 has a cross-section area equal to the area of the lens, but its center is displaced from the center of the lens. A simple calculation using the typical dimensions given in Sec. 2c shows that the loss at Lens 2 is as small as 5 per cent. It is reasonable to neglect this small loss at Lens 2.

b. General Expression for the Transmission Function

Rays passing through a disk of radius $\rho_o = (f_1 r/f_2)$ are transmitted by the optical system without loss. Rays that do not pass through this disk are not transmitted. The fraction of the light from a point source emitting isotropically in all directions and located at an arbitrary position to the left of Lens 1 which is transmitted by the optical system is equal to the fraction of the light that apparently could have come from a source in the full-transmission disk. This fraction is given by $\Omega/4\pi$, where Ω is the solid angle containing all rays passing through the point source which also pass through both the full-transmission disk and Lens 1.

There is a different expression for the transmission function in each of the three regions shown in Fig. XI-5. The transmission function for a point source in region K(K=I, II, III) is given by

$$T = T_k = \frac{\Omega_k(\rho, z)}{4\pi},$$

where (ρ, z) is the location of the point source. For a point source in region I, all rays passing through the full-transmission disk also pass through Lens 1, so $\Omega_1(\rho, z)$ is the solid angle subtended by the full-transmission disk at (ρ, z). For a point source in region II, all rays passing through Lens 1 also pass through the full-transmission disk, so $\Omega_2(\rho, z)$ is the solid angle subtended by Lens 1 at (ρ, z). For a point source in region III, the rays that are transmitted are limited by both the full-transmission disk and by Lens 1, so $\Omega_3(\rho, z)$ is the solid angle defined in Fig. XI-5.

A good approximation for the solid angles Ω_1 and Ω_2 is easily computed by using

$$\Omega_k = 2\pi(1-\cos\theta_k),$$

where θ_k is the interior half-angle of the cone of solid angle Ω_k:

$$\Omega_1(\rho, z) = 2\pi\left\{1 - \sqrt{\frac{1}{2}+\frac{1}{2}\,\frac{z^2+\rho^2-\rho_o^2}{\left[z^2+(\rho-\rho_o)^2\right]^{1/2}\left[z^2+(\rho+\rho_o)^2\right]^{1/2}}}\right\}$$

$$\Omega_2(\rho, z) = 2\pi\left\{1 - \sqrt{\frac{1}{2}+\frac{1}{2}\,\frac{(f_1-z)^2-(R-\rho)(R+\rho)}{\left[(f_1-z)^2+(R-\rho)^2\right]^{1/2}\left[(f_1-z)^2+(R+\rho)^2\right]^{1/2}}}\right\}.$$

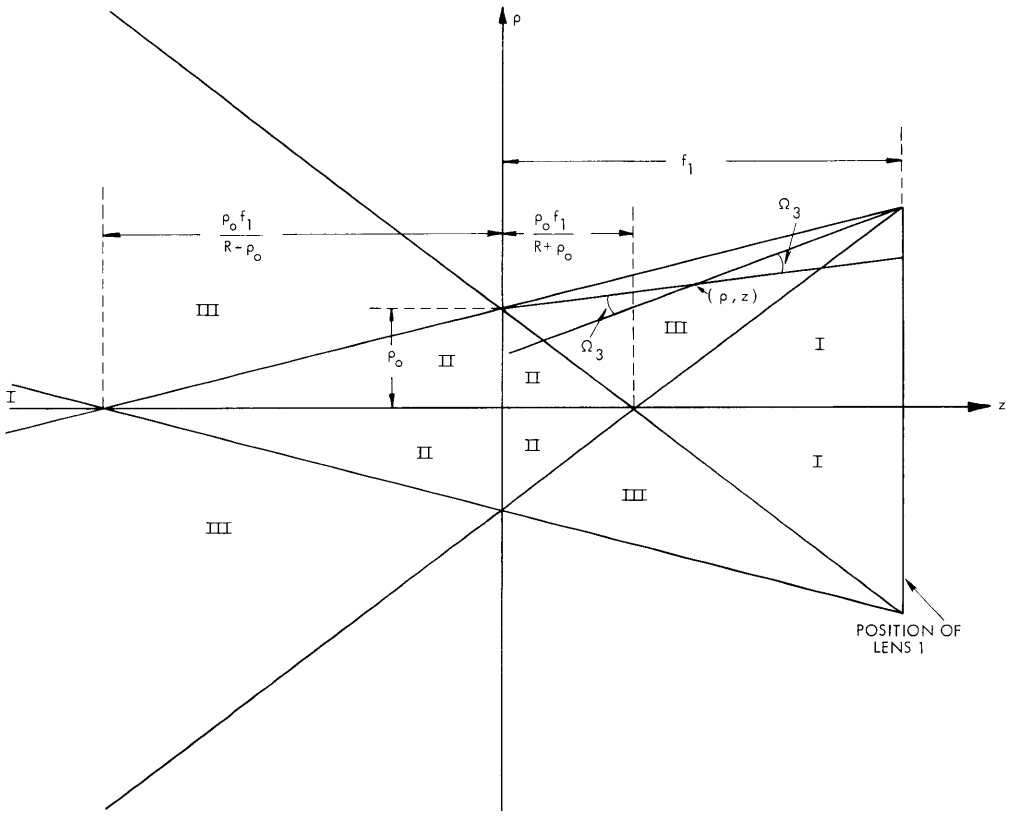

Fig. XI-5. Regions of applicability of three exact expressions for transmission function.

The expression for Ω_1 is a good approximation throughout region I, provided $R^2 \ll f_1^2$, and Ω_2 is a good approximation throughout region II, provided $\rho_o^2 \ll f_1^2$. This condition for Ω_2 is fulfilled, as long as the pinhole is small compared with the lenses.

The solid angle Ω_3 has a minimum value of zero at the outer edge of region III and a maximum value of

$$\Omega_3 = 2\pi \left\{ 1 - \sqrt{\frac{1}{2} + \frac{1}{2} \frac{f_1^2 \left(1 - \frac{rf_1}{Rf_2}\right)^2 - R^2}{f_1^2 \left(1 - \frac{rf_1}{Rf_2}\right)^2 + R^2}} \right\}$$

at the point on the z-axis which forms the common boundary of regions I, II, and III.

c. Approximate Expression for the Transmission Function

An approximation to the transmission function will now be obtained which is valid for typical geometrical conditions. The dimensions of the optical system to be used in the Fabry-Perot measurement of the profiles of lines emitted by the hollow-cathode arc discharge are $f_1 = 10$ cm, $f_2 = 20$ cm, $R = 2.5$ cm, $L = 50$ cm, $r = 1.225 \times 10^{-2}$ cm.

For these dimensions, Ω_1 and Ω_2 vary only slightly with ρ for fixed z. This can be seen by considering, for example a point (ρ, z) in region I. The solid angle Ω_1 is approximately the area of the full-transmission disk divided by the square of the distance from the point (ρ, z) to the disk, or

$$\Omega_1 \approx \frac{\pi\rho_o^2}{\rho^2 + z^2}.$$

For the dimensions given above $\rho < (1/4)z$ in region I and as ρ goes from zero to $(1/4)z$, Ω_1 changes by only 6 per cent. A similar calculation applies to Ω_2. Such a small error is made in approximating $\Omega_k(\rho, z)(k=1, 2)$ by $\Omega_k(0, z)$ because the maximum variation in ρ is much less than the distance from (ρ, z) to the disk that defines Ω_k. Thus the first approximation that we make is that all points on any cross-section disk in regions I or II have the same transmission function, $T_k(0, z)$.

For the dimensions given above it is also a reasonable approximation to neglect the contribution of the light from region III. The volume of region III is only ≈ 0.3 per cent of the volume of region I, and the transmission function for points in region III is less than the transmission function for points in region I. If the radiation source were very inhomogeneous, it might not be valid to neglect radiation from region III. For example, if the emitted intensity changes by a factor of 100 over a distance comparable to a typical dimension, ρ_o, of region III, this approximation would be invalid.

In region I, $z \geq \rho_o f_1/(R+\rho_o) \approx 4\rho_o$ for the dimensions given above, so that $z^2 \gg \rho_o^2$ and the expression for Ω_1 can be expanded, with terms of the order of $(\rho_o/z)^4$ and higher neglected. The resulting approximate expression for the transmission function is

$$T_1(\rho, z) \simeq T_1(0, z) = \frac{\Omega_1(0, z)}{4\pi} \simeq \frac{1}{4}\left(\frac{f_1}{f_2}\right)^2 \left(\frac{r}{z}\right)^2.$$

Thus in region I the transmission function decreases as $1/z^2$.

In region II $z < \rho f_1/(R+\rho_o) \approx 4\rho_o \approx 5 \times 10^{-2}$ cm, so that $z/f_1 \simeq 5 \times 10^{-3}$ cm $\ll 1$ cm, and also $\left(R^2/f_1^2\right) = 1/16 \ll 1$. The expression for Ω_2 can be expanded, with z/f_1 and $(R/f_1)^4$ and smaller terms relative to one neglected. The approximate expression for the transmission function that is obtained is

$$T_2(\rho, z) \simeq T_2(0, z) = \frac{\Omega_2(0, z)}{2\pi} \simeq \frac{1}{4}\left(\frac{R}{f_1}\right)^2.$$

Thus in region II the transmission function is independent of z. Figure XI-6 shows the transmission function for $\rho = 0$ in regions I and II as a function of z for the chosen typical conditions.

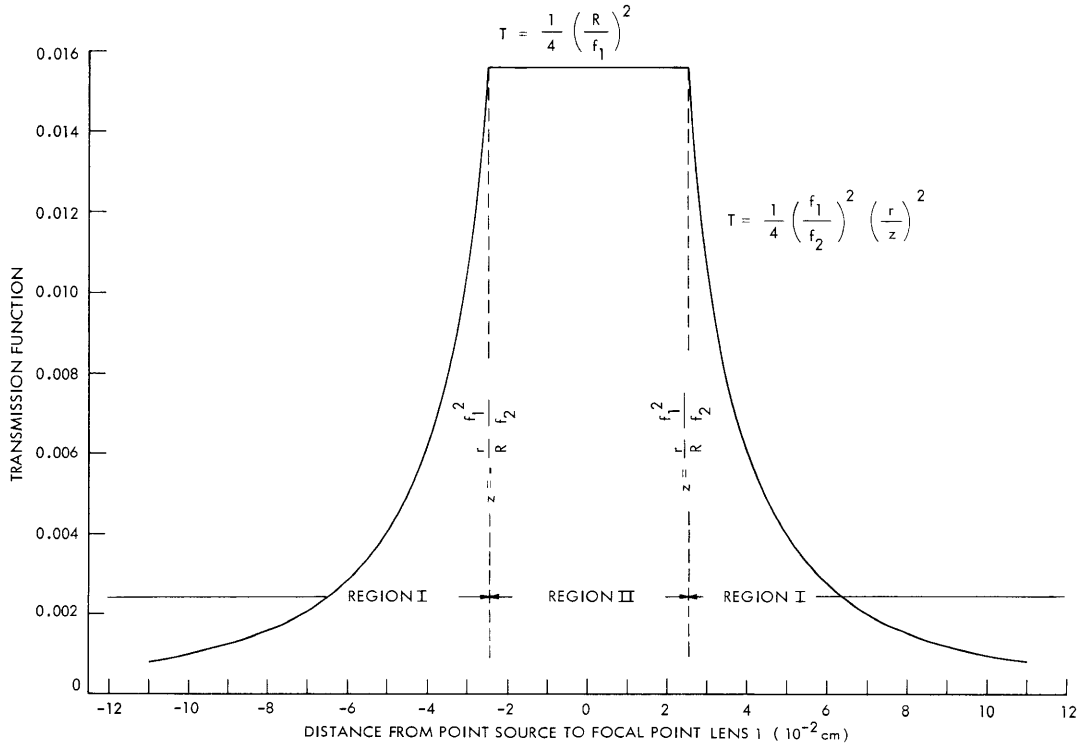

Fig. XI-6. Approximate transmission function vs distance of point source from focal point of Lens 1.

As a final approximation, ρ_o is neglected in comparison with R in the expressions giving the boundary between regions I and II. In this approximation the volume from which the optical system accepts light is symmetric with respect to the plane z = 0. The transmission function can be written

$$T(z) = T_1(z) = \frac{1}{4}\left(\frac{f_1}{f_2}\right)^2 \left(\frac{r}{z}\right)^2 \qquad |z| \geq \frac{r}{R}\frac{f_1^2}{f_2}$$

$$T(z) = T_2(z) = \frac{1}{4}\left(\frac{R}{f_1}\right)^2 \qquad |z| \leq \frac{r}{R}\frac{f_1^2}{f_2}.$$

Note that the transmission function for a point in region I depends on the size of the pinhole, while the transmission function for a point in region II depends upon the size of the lenses. The transmission function for a point source anywhere in region II is the same as the transmission function for a point at the origin (that is, at the focal point of Lens 1). $T_2(z)$ is independent of the size of the pinhole because the cross-section area, at the plane of the pinhole, of a pencil of rays from a point source in region II is smaller than the pinhole. The size of region II is determined by the radius of the pinhole. Hence the total light intensity transmitted by the optics from region II in an extended source decreases with decreasing pinhole size, as is shown below.

$T_1(z)$ does not depend on the size of the lenses because the pinhole only transmits rays from a source in region I which pass through the full-transmission disk.

3. Application to Plasma Measurements

The approximate expression for the transmission function obtained above will be used here to determine the performance of the optical system of Fig. XI-3 in optical measurements on plasmas. The contributions of regions I and II of Fig. XI-5 to the intensity of light through the pinhole are computed for a uniform slab of plasma. For a cylindrical plasma in which the light flux from a unit volume varies parabolically with radius, it is shown that the Abel inversion can be used to determine the spatial distribution of light emission. For a cylindrical plasma in which the emitted intensity per unit volume is a general function, a numerical method must be used. To obtain the spatial distribution of a line profile, the power (light flux) emitted by a unit volume must be determined as a function of position at several wavelengths within the line breadth.

a. Uniform Plasma Slab

A computation of the contributions of regions I and II to the intensity of the light passing through the pinhole for a uniform slab of plasma will now be presented. The slab has thickness 2a and is centered at z = 0, that is, at the focal point of Lens 1. The power radiated by unit volume of the slab is taken to be unity. The power through the pinhole is given by

$$I = \int_V A(z)\, dxdydz = \int_{-a}^{+a} A(z)\, T(z)\, dz,$$

where A(z) is the area perpendicular to the z-axis of an elemental volume Adz, and V is the volume common to the plasma and the region from which light is accepted by the optical system. Using the approximations of Sec. 2c, the power of the light from region I transmitted by the pinhole is

$$I_1 = 2\int_{\frac{rf_1^2}{Rf_2}}^{a} T_1(z)\,A(z)\,dz = \frac{\pi}{2}\left(\frac{Rf_1}{f_2}\right)^2 \int_{\frac{rf_1^2}{Rf_2}}^{a} \frac{1}{z^2}\left(z - \frac{rf_1^2}{Rf_2}\right)^2 dz$$

$$\simeq \frac{\pi}{2}\left(\frac{Rf_1}{f_2}\right)^2 a.$$

In evaluating the integral, terms of the order of $\frac{1}{a}\left(\frac{rf_1^2}{Rf_2}\right)^2$ have been neglected as compared with a, which is less than 1 per cent error for $a > 0.25$ cm. The power of the light from region II transmitted by the pinhole is $I_2 = T_2 V_2$, where V_2 is the volume of region II. Hence

$$I_2 = \frac{\pi}{6}\left(\frac{f_1}{f_2}\right)^2 \frac{r^3 R}{f_2}.$$

The ratio of the power from the small region II near the origin to the power from the rest of the plasma is

$$\frac{I_2}{I_1} = \frac{1}{3}\frac{f_1^2 r}{f_2 RA} \approx \frac{1}{120a}.$$

Thus $(I_2/I_1) < 3\%$ for $a > 0.25$ cm. Most of the light comes from the plasma in region I, despite the fact that the transmission coefficient is much smaller for a point in region I than for a point in region II. This is so because the volume of region I is much greater than that of region II. The ratio of the volumes $(V_1/V_2) > 10^3$ for $a > 0.25$ cm.

b. Cylindrical Plasma – Parabolic Distribution of Emission Intensity

A cylindrical plasma in which the power radiated per unit volume falls off parabolically with increasing distance from the axis will be considered here. The geometry is shown in Fig. XI-7. The axis of the plasma lies along the y-axis of the rectangular coordinate system. The plasma radius is b. The axis of the optical system is parallel to the z axis with the focal point of Lens 1 at $(x_s, 0, 0)$. Light is collected from the shaded region of the plasma. The power emitted by a unit volume of plasma is

$$\epsilon(r) = \left(1 - \frac{r^2}{b^2}\right),$$

where $r^2 = x^2 + z^2$.

If $\epsilon(r)$ does not drop off too rapidly with r, that is, for sufficiently large b, several simplifications can be made which permit the Abel integral inversion to be used. These approximations are valid to better than 1 per cent accuracy when $b > 0.25$ cm. For this condition, the contribution to the total intensity transmitted by the optical system from region II can be neglected for the typical dimensions used in Sec. 2c, even when the optical axis passes through the center of the plasma. Also, the emission per unit volume from all points on the disk shown in Fig. XI-7 can be taken to be $\epsilon(\bar{r})$, where $\bar{r} = \sqrt{z^2 + x_s^2}$. This means that the intensity emitted at any point on this disk is the same as the intensity emitted on the optical axis. Thus the power transmitted by the optical system is

$$I(x_s) = 2 \int_0^{z_m} \epsilon\left(\sqrt{z^2 + x_s^2}\right) A(z)\, T(z)\, dz = 2 \int_0^{z_m} \left(1 - \frac{z^2 + x_s^2}{b^2}\right) A(z)\, T(z)\, dz,$$

where $z_m = \sqrt{b^2 - x_s^2}$. This approximation for the upper limit of integration is the same as the standard approximation made when using the Abel inversion. It can be seen by referring to Fig. XI-7 that this assumption approximates the curved surface

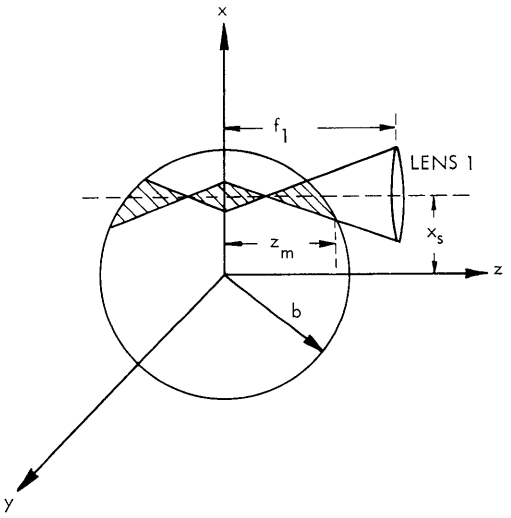

Fig. XI-7. Geometry for cylindrical plasma.

of the cylinder by a number of disk-shaped plane elements parallel to the x-y plane whose centers are at the intersection of the optical axis and the surface of the cylinder. This is a valid approximation because the cone of acceptance of the optical system is slender (the tangent of its interior half-angle is approximately 1/4). Moreover, the region of the volume of acceptance which is influenced by the approximation is the region

in which the emission intensity is small. Writing the lower limit of the integral as zero extends region I up to the x-y plane, an approximation that in part offsets neglecting light from region II.

The integral for $I(x_s)$ can be written in terms of r as

$$I(x_s) = \frac{\pi}{2}\left(\frac{Rr}{f_2}\right)^2 \int_{x_s}^{b} \frac{\epsilon(\bar{r})\,\bar{r}\,d\bar{r}}{\sqrt{r^2 - x_s^2}}$$

by using the relation $\bar{r}^2 = z^2 + x_s^2$. The power radiated per unit volume $\epsilon(\bar{r})$ can be found by means of the Abel inversion. It is

$$\epsilon(r) = -\frac{2}{\pi^2}\left(\frac{f_2}{Rr}\right)^2 \int_{r}^{b} \frac{I'(x_s)\,dx_s}{\sqrt{x_s^2 - r^2}}.$$

The factor $\frac{2}{\pi^2}\left(\frac{f_2}{Rr}\right)^2$ displays the influence of the particular optical system considered in these calculations. In most experiments in which the Abel inversion is used to obtain the space distribution of light emission, the cross section of the acceptance volume of the optics is independent of z, and the factor $\frac{2}{\pi^2}\left(\frac{f_2}{Rr}\right)^2$ is simply $\frac{1}{\pi}$ times the reciprocal of the slit-area connected with the experiment.

c. Cylindrical Plasma – General Distribution of Emission Intensity

Here, the case of a cylindrically symmetric plasma in which the power radiated per unit volume is a general function of the radial coordinate is considered. The geometry is the same as that above and is shown in Fig. XI-7. For this case, the power transmitted by the optical system is

$$I(x_s) = \iiint_V dx\,dy\,dz\;\epsilon(r)\;T(z),$$

where V is the volume common to the acceptance region of the optical system and the plasma. This equation can be rewritten

$$I(x_s) = \left(\frac{R}{f_1}\right)^2 \int_0^{\frac{\rho_o f_1}{R}} h(z, x_s)\,dz - \left(\frac{f_1 r}{f_2}\right)^2 \int_{\frac{\rho_o f_1}{R}}^{z_m} h(z, x_s)\,\frac{dz}{z^2},$$

where

$$h(z,x_s) = \int_{x_s-\rho_o+\frac{Rz}{f_1}}^{x_s+\rho_o-\frac{Rz}{f_1}} dx \quad \sqrt{\left(\rho_o-\frac{Rz}{f_1}\right)^2-(x-x_s)^2}\ \epsilon(r).$$

The first integral in the expression for $I(x_s)$ is the contribution from region II, and the second integral is the contribution from region I. The expression for $h(z,x_s)$ is derived under the assumption that the emission from the regions of the plasma near the surface may be calculated by approximating the plasma volume elements in this region by disk-shaped plane elements parallel to the x-y plane, as in the preceding section. Therefore, if the plasma is b, $z_m = \sqrt{b^2-x_s^2}$.

In this case it is possible to determine $\epsilon(r)$ by assuming that it is given by a power series, $\epsilon(r) = \sum_{n=0}^{N} c_n\left(x^2+z^2\right)^n$, and substituting this in the integrals above. This substitution yields a set of linear equations, of which the left-hand sides are the measured values of $I(x_s)$, and the right-hand sides are linear summations containing the coefficients c_n. These coefficients are determined by solving this set of equations with the aid of a computer.

These calculations will be applied to measurements that are to be made on a DC hollow-cathode arc.

J. D. Silk, J. C. Ingraham

D. MICROWAVE SCATTERING FROM AN ELECTRON-BEAM PRODUCED PLASMA

Observations have been made of the scattering of microwaves from electron density fluctuations in a plasma produced by an electron beam. The nature of the fluctuations is not yet clear, but the most likely possibility is that they are longitudinal plasma waves excited by the beam.

The theory of density fluctuations in plasmas and the scattering of electromagnetic radiation from these fluctuations has been analyzed by Fejer,[1] Ichimaru,[2] and Salpeter.[3] The frequency of the scattered radiation is shifted from the incident frequency by ±f, where f is the frequency of the density fluctuation responsible for the scattering. The amplitude of the scattered radiation is approximately proportional to the potential energy of the density fluctuation. Scattering of electromagnetic waves from plasmas provides a method for investigating the spectrum of density fluctuations, and scattering experiments have been carried out to investigate both thermal fluctuations[4] and large-amplitude fluctuations associated with unstable plasma waves.[5]

In our experiment radiation at an X-band frequency was incident on the plasma from a waveguide, and a separate waveguide picked up the radiation that was scattered by the plasma. The scattered radiation was shifted in frequency from the incident radiation

by the frequency of the density fluctuations which were observed independently by means of probes inserted into the plasma.

The experimental tube is illustrated in Fig. XI-8. The electron gun, located at one end of the tube, fires an electron beam into argon gas and ionized it. The axis of the

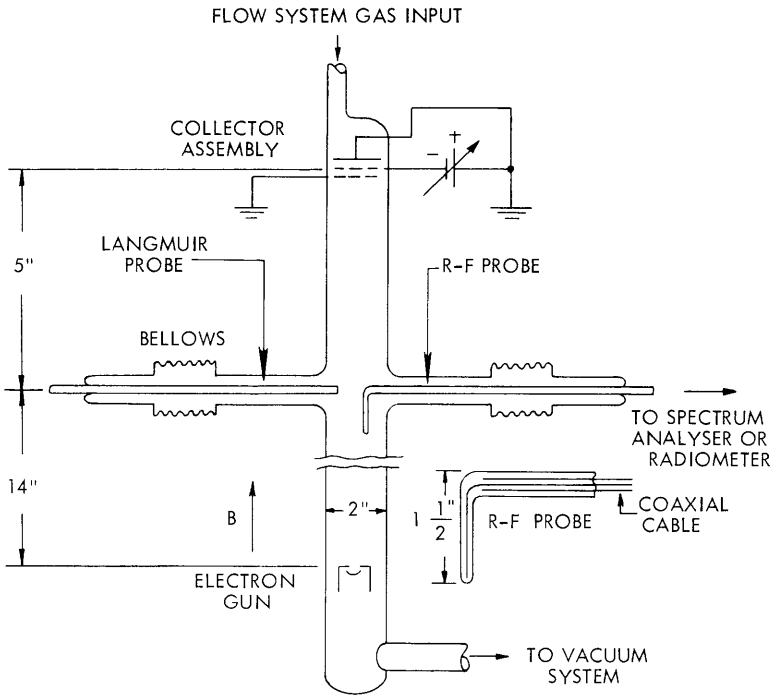

Fig. XI-8. Experimental tube.

tube is aligned along a uniform magnetic field, but the electron gun is shielded from the field, so that the beam electrons acquire transverse energy as they enter the magnetic field. There are two probes, a guard-ring Langmuir probe and an RF probe, which can be moved radially into the plasma by means of bellows. The RF probe is a coaxial cable enclosed completely in glass so that it draws no DC current from the plasma. At the far end of the tube is a collector assembly which consists of a flat circular plate with two grids in front of it. The grids could be biased to determine the axial velocity of the electron beam, but, for this experiment, the entire assembly was grounded as was the anode of the gun so that no axial electric field existed in the main section of the tube. Two pieces of X-band wave guide are mounted with their axes perpendicular to the axis of the tube as shown in Fig. XI-9. A block diagram of the experimental apparatus is shown in Fig. XI-10.

Both the RF probe and the Langmuir probe could be connected to a spectrum analyzer, and signals from each of them exhibited maxima at roughly the same

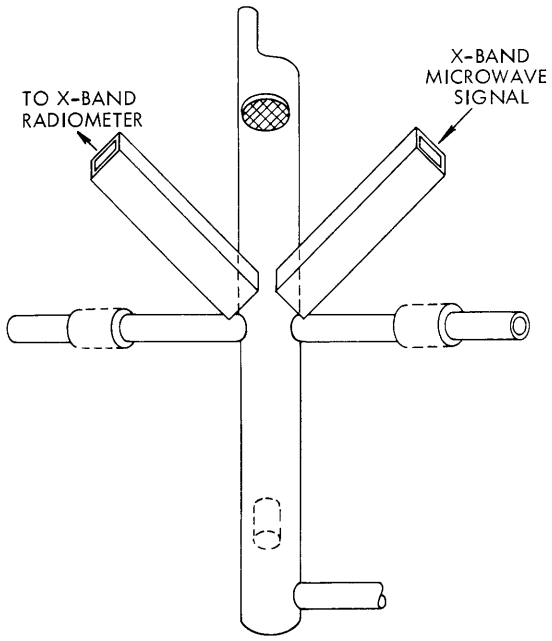

Fig. XI-9. Scattering geometry.

frequencies. A peak was observed whose frequency could be varied from approximately 200 Mc to 400 Mc by varying the gas pressure, magnetic field, and beam voltage and current. The frequency of the peak increased whenever the value of any of these parameters was increased, the others being held constant. The magnetic field was of the order of 250 Gauss, so the cyclotron frequency was approximately 700 Mc. Since the observed peak was well below this value, it could not be

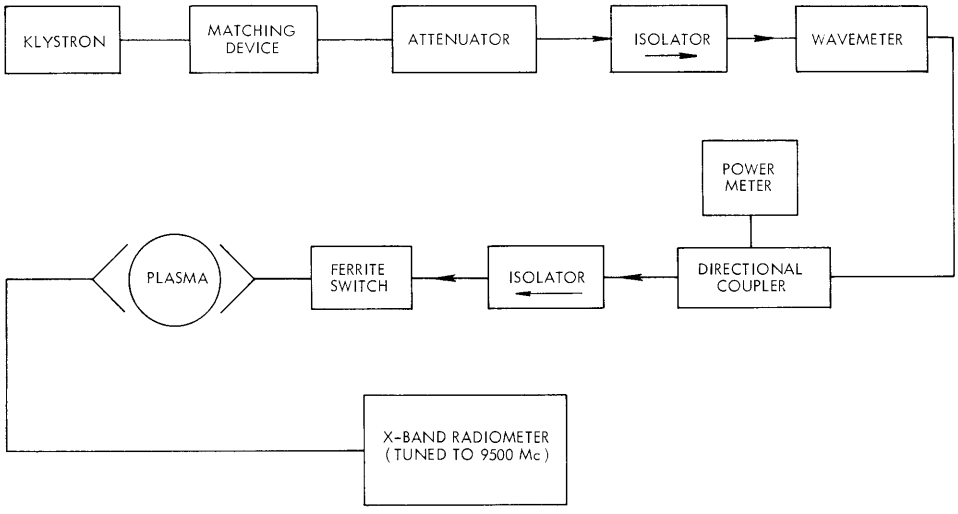

Fig. XI-10. Diagram of the experimental apparatus.

interpreted as cyclotron radiation, nor could it be associated with the resonance at the upper hybrid frequency, $\omega = \sqrt{\omega_c^2 + \omega_p^2}$. The frequency values 200-400 Mc were reasonable values, however, for an assumed plasma frequency.

The radiometer detected microwave radiation at f_o = 9500 Mc coming from the plasma whenever all of the following conditions were satisfied.

1. Microwave radiation at frequency f_{inc} was incident on the plasma.
2. A disturbance at frequency f_{fluc} existed in the plasma, this signal being picked up by the RF probe and displayed on a spectrum analyzer.
3. The relation $f_o = f_{inc} + f_{fluc}$ was satisfied.

The frequency of the incident microwave radiation was varied, keeping the power constant, and the radiometer output was plotted against $\Delta f = f_o - f_{inc}$. The results from two separate data runs are shown in Fig. XI-11 by the dashed and solid lines. Also shown in Fig. XI-11 is the direct display on the spectrum analyzer of the fluctuation signal as seen by the RF probe.

The following comments should be made regarding Fig. XI-11.

1. The multiple peaks in the spectrum-analyzer display of the signal picked up by the RF probe were found to be instrumental. This fine structure resulted from standing waves in the coaxial cable connecting the RF probe to the spectrum analyzer. Considerable fine structure was also seen in the scattering data with somewhat different experimental parameters, and an effort will be made to determine whether this is also instrumental or if it can be related to standing waves in the plasma resulting from the finite geometry.

2. The base line for the scattering peaks falls well below zero. This is an instrumental effect caused by radiation at 9500 Mc in the wings of the incident klystron signal leaking through the ferrite switch and being detected by the radiometer. This effect was later corrected by placing a transmission cavity tuned to the incident frequency in the line between the klystron and the ferrite switch.

3. The scattering data indicated by the dashed line were taken approximately one hour after the data indicated by the solid line. The change in amplitude of the scattered signal may be associated with a drift in the experimental pressure or with a change in the emission from the electron gun.

It was observed that the noise signal from the plasma and the scattering effect disappeared suddenly when the gas pressure exceeded a critical value of $\approx 10^{-4}$ mm Hg. Although no measurements of electron density and temperature were made for the plasma because of the poisoning of the cathode, the Langmuir probe was moved through the electron beam to determine its cross section when no gas was present. The beam current and voltage were also measured, and the electron density of the beam was calculated from the relation $i = N_b$ evA. This gave $N_b = 1.4 \times 10^8$ electrons/cm^3. If the

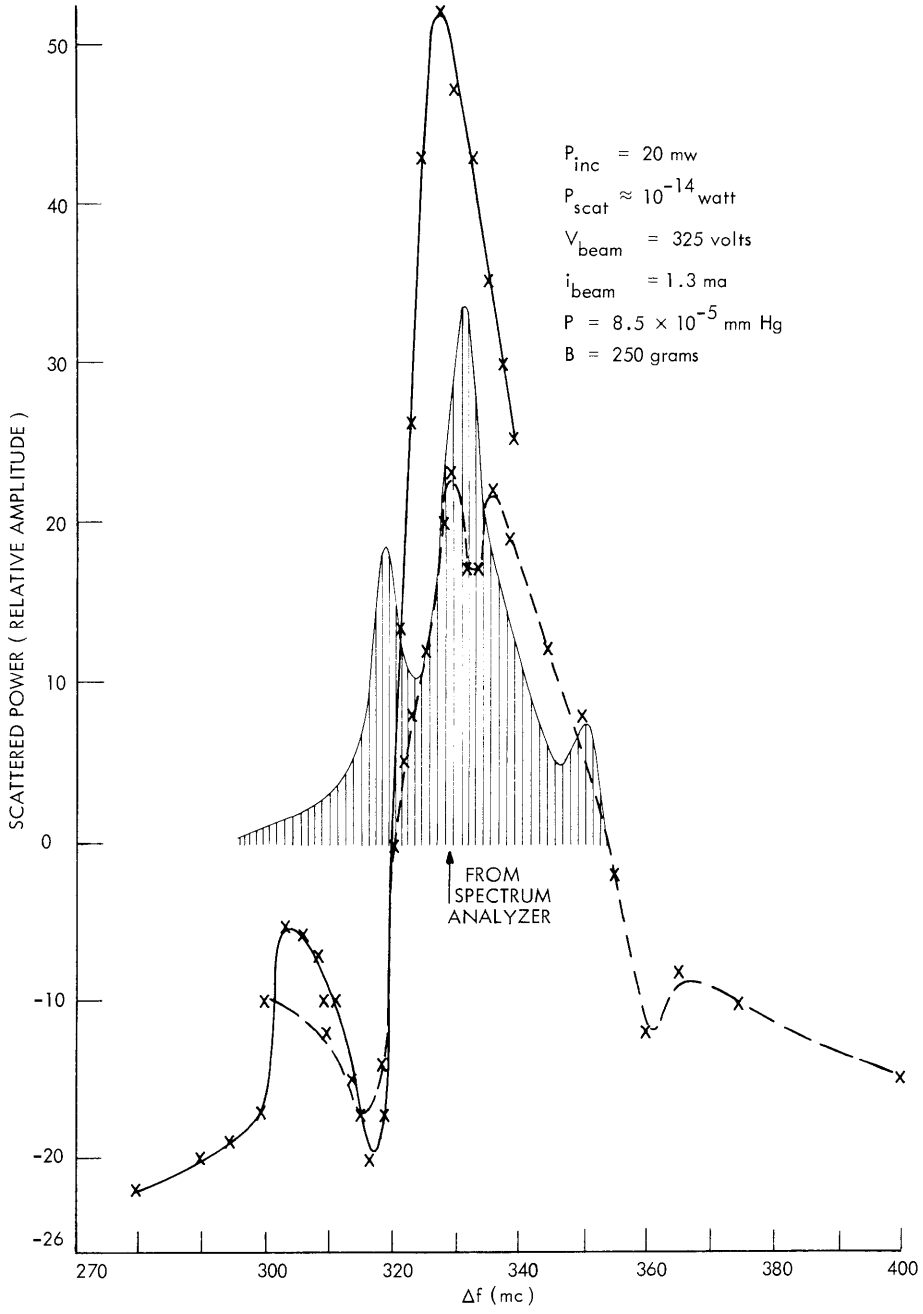

Fig. XI-11. Scattered microwave power and RF probe power vs frequency.

total electron density (plasma plus beam) were $\approx 1.1 \times 10^9$ electrons/cm^3 when argon gas at a pressure of 8.5×10^{-5} mm Hg was present, the plasma frequency would be 330 Mc/sec, equal to the frequency of the observed signal.

Since quantitative measurements were not made, comments regarding the nature of the disturbance in the plasma from which the scattering occurred can only be speculative. The observations above suggest, however, the possibility that the scattering was from electron density fluctuations associated with a longitudinal plasma wave, which was unstable because of a coupling with the electron beam, the instability becoming quenched when damping caused by electron neutral collisions became too high.

R. L. Kronquist

References

1. J. A. Fejer, Can. J. Phys. 38, 1114-1133 (1960).
2. S. Ichimaru, Ann. Phys. (N.Y.) 20, 78-118 (1962).
3. E. E. Salpeter, Phys. Rev. 120, 1528-1535 (1960).
4. K. L. Bowles, Phys. Rev. Letters 1, 454 (1958).
5. V. Arunasalam and S. C. Brown, Phys. Rev. 140, A471 (1965).

E. BUBBLE WINDOWS FOR FAR INFRARED RADIATION

Plasma tubes used in far infrared experiments (0.1 mm $< \lambda <$ 1.0 mm) are usually equipped with crystal quartz windows, because of the high transmission of crystal quartz in this spectral region.[1] Since radiant energy is at a premium at far infrared wavelengths, this advantage of crystal quartz usually outweighs such a disadvantage as not being able to fuse the windows onto the plasma tube envelope. (They are usually mounted with rubber O-ring type assemblies.) Fused quartz does not have this disadvantage, but its transmission is significantly lower than that of crystal quartz.[1] Another consideration is important, however, in comparing these two materials. It has been shown by Filippov and Yaroslavskii[2] that the transmission of crystal quartz changes with temperature, whereas that of fused quartz does not. For example, at 150-μ wavelength, the transmission of a plate of crystal quartz, 2 mm thick, changes from ~75 to ~71% for a temperature change from 300°K to 350°K. This represents more than a 5% decrease in transmission. The transmission of an equally thick plate of fused quartz remains constant at ~25% for the same temperature change. The temperature dependence of crystal-quartz transmission may be a significant disadvantage in some experiments. For example, in an emission or propagation experiment in which the plasma heats the windows and the far infrared power level measured with the plasma on is compared with the level measured with the plasma off. Of course, changes in

window transmission become increasingly important, the more passes the radiation makes through the windows.

In experiments in which the temperature dependence of crystal-quartz transmission is important, fused-quartz windows should be used in spite of their lower transmission. To overcome the disadvantage of the lower transmission, the windows must be as thin as possible; however, relatively large windows are usually necessary, since energy considerations usually require far infrared beams of large area. Thus a large, thin window must form part of the wall of the evacuated plasma chamber. Such a window, if it is flat, would collapse under atmospheric pressure unless supported internally, possibly by a metallic grid of some kind. An alternative is a thin-walled quartz bubble blown inward (convex toward the low-pressure region), so that it is always under tension when subjected to the large pressure differential. If properly constructed, such a window can be self-supporting and extremely thin (a few thousandths of an inch thick), and may have far infrared transmission coefficients comparable to or larger than those of typical crystal-quartz windows. Such a bubble window is similar to those sometimes used on nuclear counters.

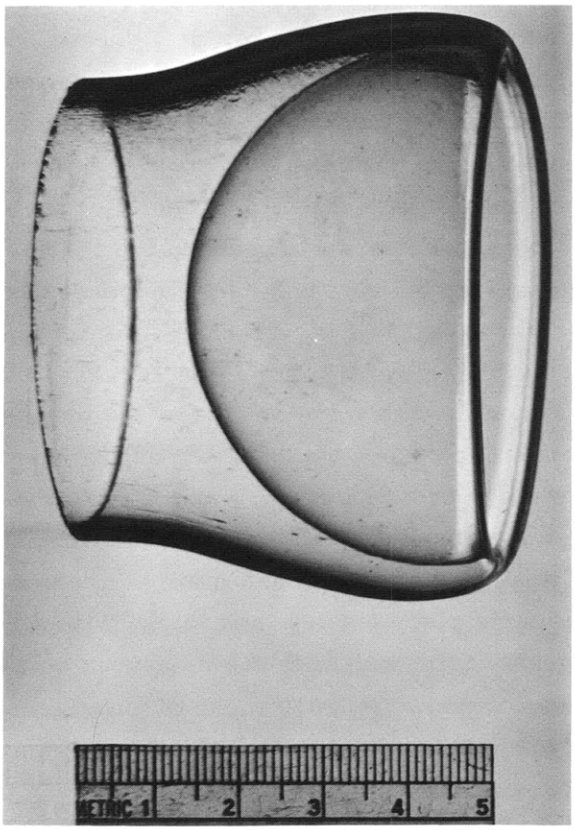

Fig. XI-12. Photograph of the bubble window.

Figure XI-12 shows a bubble window that has been constructed.[3] The diameter of the bubble opening is 5.8 cm. The bubble is approximately 0.0045 inch thick in the region that would be traversed by a 5-cm diameter beam (the beam size for which the bubble was constructed), varying from ~0.00425 inch in a few regions near the center to ~0.006 inch in some regions, particularly near its periphery. The ability of this window to withstand atmospheric pressure when evacuated has been tested and verified.

The imperfections visible in the photograph are, for the most part, on the quartz wall surrounding the bubble rather than on the bubble itself. On the bubble, however, there are "draw lines" characteristic of drawn quartz and some small but visible bubbles and inclusions. The image distortions produced by these imperfections should be of little consequence in most plasma emission or absorption experiments.

The far infrared transmission of this window has been measured from wave number ($\nu \equiv 1/\lambda$) $\nu \approx 3$ cm^{-1} ($\lambda \approx 3.33$ mm) to $\nu \approx 55$ cm^{-1} ($\lambda \approx 182$ μ) by using a far infrared Michelson interferometer.[4] Some results of these measurements are shown in Fig. XI-13, in which the three curves correspond to three different positions of the window in the interferometer. The rapid fluctuations are due to such effects as instrumental noise and are unrelated to window properties. Each of the curves represents the ratio of two spectra, one obtained with the window in the optical path of the instrument (numerator), the other with the window removed (denominator). In all cases an aperture of 4-cm diameter was kept fixed, close to the window location, in order to define a beam and to eliminate any effects that the outer edges or walls of the window might have on the transmitted radiation. Curves a and b correspond to a window location between the beam splitter and detector of the interferometer (the window was ≈13 inches from the detector). Curve a corresponds to the beam 'coming out' through the window, (left to right in Fig. XI-12), and curve b corresponds to the beam 'going in' through the window (right to left in Fig. XI-12). As might be expected, there is no apparent difference between these two transmission curves. Curve c corresponds to a window position between the mercury arc source of the interferometer and the beam splitter with the beam 'coming out' of the window, as for curve a. In all cases the transmission varies between approximately 70% and 90%.

All three curves show the channel spectrum produced by interference of internally reflected radiation. The spacing of maxima and minima agree reasonably well with what would be expected for a quartz slab, 0.0045 inch thick, with a refractive index of 1.95. This refractive index agrees quite well with the measured value for fused quartz.[5] It was found that for thicker windows (~0.010 inch) of similar over-all dimensions the channel spectrum tends to disappear, with the transmission remaining fairly flat at ~80%. This value is approximately the same as the average value of the transmission curves (Fig. XI-13) of the thinner window; this suggests that transmission losses are due primarily to reflection rather than absorption.

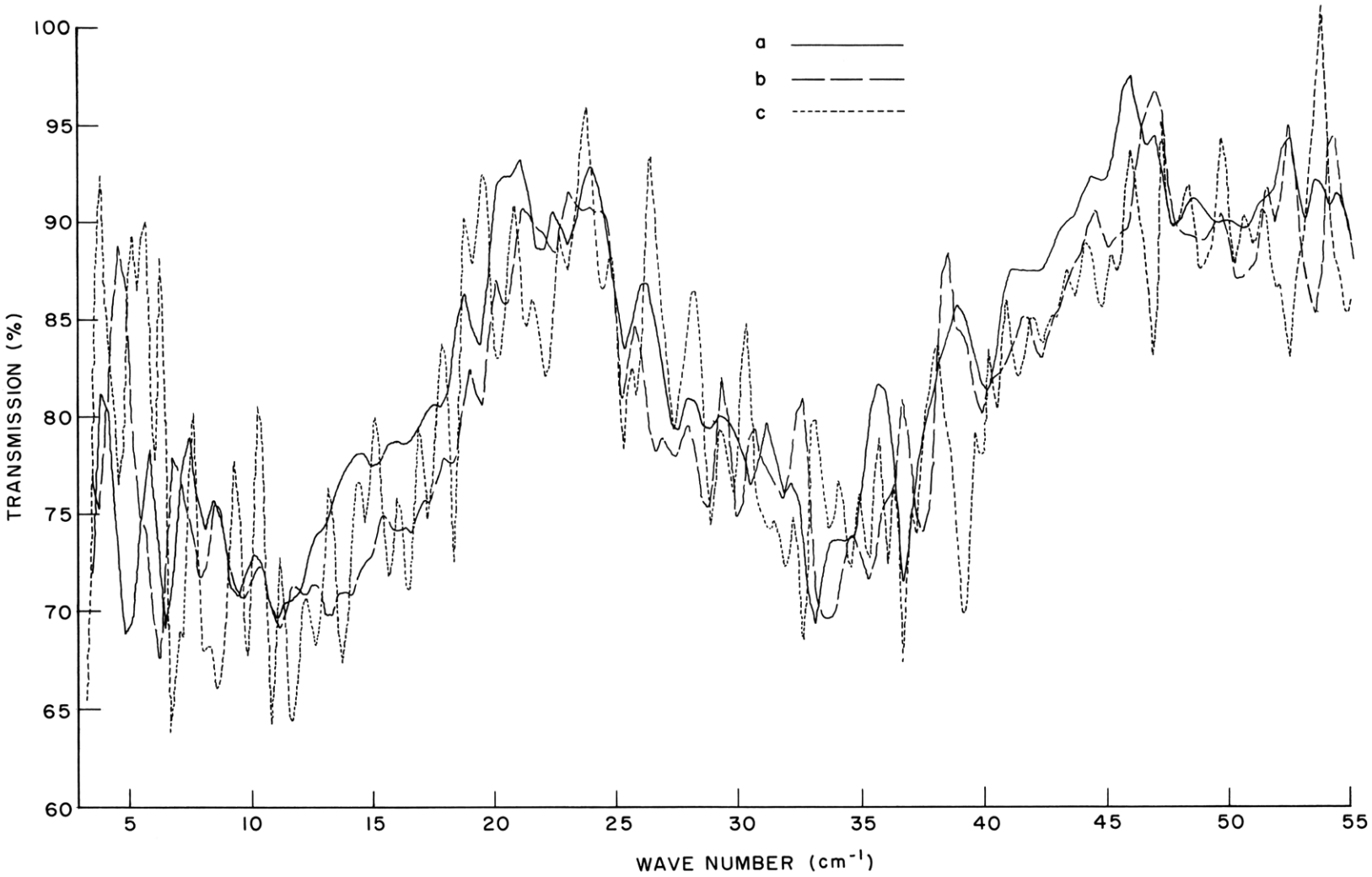

Fig. XI-13. Transmission spectra of the bubble window.

A window of this type might be expected to act as a negative meniscus lens, a diverging lens (thinner at the center than at the edges) with the centers of curvature of both surfaces located on the same side of the lens. Any beam divergence, or "lens effect," should appear as a decrease in transmission when the window is moved farther from the detector. Curve c shows the transmission of the window when it is located almost three times farther from the detector than for curves a and b. No lens effect is apparent in these measurements. A lens effect is not observed because the window, although it has significant curvature, is extremely thin and its thickness is reasonably uniform over the region traversed by the beam.

The effect of the window in phase-shift measurements (e. g. , window in one arm of the interferometer) has not been checked. Any such effect is of no consequence for the present intended application of the window, which involves only its power-transmission properties.

The effect of the window on an arbitrary ray is not very different from that of a flat slab of the same thickness, since the surface normal at the point of incidence on one surface is almost parallel to the normal at the point of emergence from the other surface. Consequently, the effect of the window is to shift the ray laterally because of its finite thickness, and to give the emerging ray only a slight angular displacement with respect to the incident ray. Clearly, both of these effects are small; however, since the angular displacement, unlike the lateral displacement, causes a point along the ray to deviate from its original position (i. e. , with no window present) increasingly as the

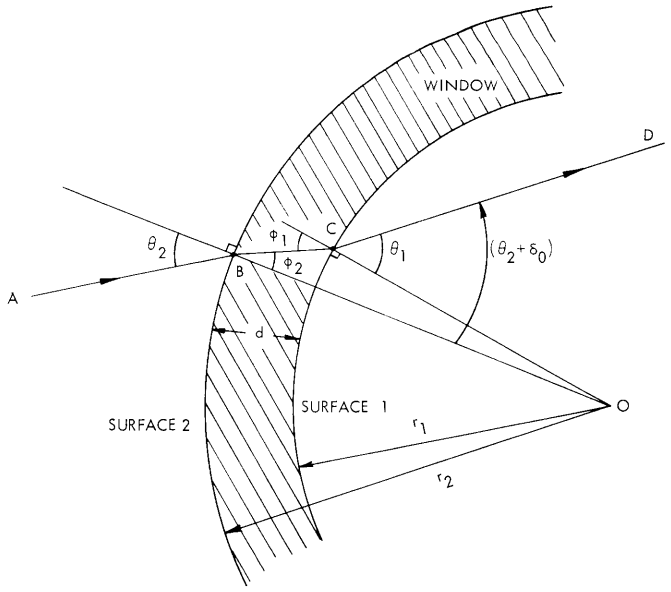

Fig. XI-14. Geometrical construction for calculating ray divergence.

distance from the window increases, an estimate of the magnitude of this effect would be valuable.

In Fig. XI-14 ABCD is an arbitrary ray, and the shaded region represents the window. Its thickness, d, is small compared with the radii of curvature (r_1, r_2; $r_1 < r_2$) of its surfaces, which are assumed to be spherical and concentric. θ_2 and θ_1 are the (external) angles of incidence and emergence, respectively; ϕ_2 and ϕ_1 are the (internal) angles of refraction and incidence at surfaces 2 and 1, respectively. It can be shown quite easily that the angle δ_o between the outgoing ray (CD) and the incident ray (AB) is given by

$$\delta_o \approx \frac{d}{r_1}(\tan\theta_2 - \tan\phi_1). \tag{1}$$

For a ray traveling in the reverse direction (DCBA) the angular deviation measured with respect to surface normal CO is

$$\delta_i \approx -\frac{d}{r_2}(\tan\theta_1 - \tan\phi_1). \tag{2}$$

Since in both cases $\theta_{1,2} > \phi_{1,2}$, δ_o is always positive, and δ_i is always negative, thereby indicating that for a ray incident on the outer surface (δ_o) the emerging ray deviates away from the direction of the surface normal, and for a ray incident on the inner surface (δ_i) the ray deviates toward the direction of the surface normal. The magnitudes of the angular deviation are approximately equal in both cases. This means, for example, that a bundle of rays initially parallel to the window axis would diverge if incident on the window from either side, as expected.[6] From Eq. 1, we find that for a window refractive index of 1.95, d = 0.005 inch, r_1 = 1 inch, and $\theta_2 = 60°$, we get $\delta_o \approx$ 6.2 mrad; this implies that a parallel beam initially of 5-cm diameter will diverge to a diameter of only ~6.24 cm at a distance of one meter beyond the window.

Reflection losses from the curved window become significant only near its periphery where the incoming light rays have large angles of incidence. Figure XI-15 shows the reflectance for a dielectric material with a refractive index of 1.95 as a function of angle of incidence. These reflectances were calculated by means of the Fresnel reflection formulas for an air-dielectric interface. $\rho_\perp$ and $\rho_\parallel$ are the reflectances for radiation polarized perpendicular to and parallel to the plane of incidence, respectively. $\bar{\rho}$ is their average value, which is characteristic of unpolarized light. $\bar{\rho}$ is also characteristic of a polarized beam that is uniform both in intensity and polarization over an annulus on the window given by a fixed value of θ. In this case, $\bar{\rho}$ represents the average reflectance of the annulus.

Figure XI-15 also gives the internal reflection loss at the second dielectric-air interface of θ is identified with the angle of refraction at that surface (i.e., the angle between

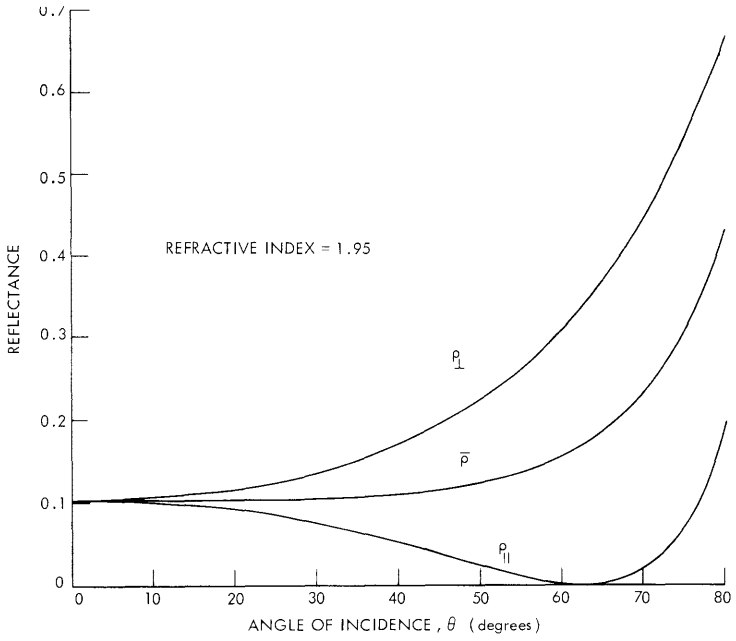

Fig. XI-15. Calculated reflectance of the fused-quartz surface.

the outgoing ray and surface normal). Because the window is very thin, this angle is approximately equal to the angle of incidence at the first boundary; this indicates that the percentage power loss by reflection is approximately the same at both boundaries.

The reflection loss remains fairly constant at small angles and does not become significant until $\theta > 60°$ (at $\theta \approx 60\%$, $\bar{\rho} \approx 15\%$). For the window shown in Fig. XI-12 all rays in a 5 cm diameter beam of parallel light have angles of incidence $\theta \leq 60°$. In connection with the reflection effects of the window it should be noted that the curvature of the window causes most of the reflected radiation to be directed out of the beam rather than back into the beam. This can be a definite advantage in some experimental situations.

The transmission measurements discussed in this report were made with the generous assistance of D. T. Llewellyn-Jones, both in the operation of his interferometer and in the processing of the data.

G. L. Rogoff

Footnotes and References

1. T. K. McCubbin, Jr., and W. M. Sinton, J. Opt. Soc. Am. 40, 537 (1950).
2. O. K. Filippov and N. G. Yaroslavskii, Opt. Spectry. (USSR) 15, 299 (1963).
3. This bubble window was constructed by G. B. Finkenbeiner of G. Finkenbeiner, Inc., 23 Alaska Avenue, Bedford, Massachusetts. The material used was "Vitreosil" (trade name) obtained from Thermal American Fused Quartz Co., Route 202 and Change Bridge Road, Montville, New Jersey.
4. D. T. Llewellyn-Jones, Quarterly Progress Report No. 74, Research Laboratory of Electronics, M.I.T., July 15, 1964, pp. 81-89.

5. R. Geick, Z. Physik, 161, 116 (1961).

6. Although the sign of δ is different for the two directions of propagation of a given ray, the position of the surface normal to which δ is referred changes from, say, above the emergent ray for one direction of propagation to below the emergent ray for the other direction of propagation. Thus the emergent ray in both cases diverges from the window axis.